Electronic Supplementary Information

Laves Phase Ir$_2$Sm Intermetallic Nanoparticles as a Highly Active Electrocatalyst for Acidic Oxygen Evolution Reaction

Shuai Zhang, Leilei Yin, Qingqing Li, Siyuan Wang, Weihua Wang and Yaping Du*

Experimental Procedures

Chemicals

$H_2IrCl_6 \cdot 6H_2O$ (Ir ≥35%, Aladdin), Nafion solution (5 wt.%, Alfa), CN_2H_2 (99%, Sigma-Aldrich), $SmCl_3$ (99.99%, Adamas), Na (99.7%, Aladdin), 2-propanol (99.9%, Aladdin), ultradry tetrahydrofuran (99.9%, Aladdin), graphene (The Six Element, Inc.), H_2SO_4(98%, Sinopharm), Ir/C (10 wt.%, Aladdin), Milli-Q water (≥18.2 MΩ·cm). All the chemicals were used without further purification.

Catalyst Synthesis

0.3 g $H_2IrCl_6 \cdot 6H_2O$, CN_2H_2, $SmCl_3$ (the mole ratio of Ir, Sm, and CN_2H_2 were 5: 3: 80) and 0.45 g graphene were mixed in an agate mortar. The obtained mixture was then transferred into a boron nitride (BN) crucible for heat treatment. Then a Na ingot was placed in another BN crucible. These BN crucibles were placed together in a big BN crucible (ca. 20 cm^3 inner volume) so that the sodium vapor produced would contact the powder mixture only when heated. All the heat treatment of the sample was performed under inert gas (argon). The temperature was increased to 600 °C at the rate of 5 °C min^{-1}. After the heat treatment, the powder samples were washed with 2-propanol to remove residual sodium, and the remaining sodium in the BN crucible is recycled. The obtained product was transferred to the air and leached in 500 mL of 0.5 M H_2SO_4 at 40 °C for 1 h under continuous stirring. The product was then thoroughly washed with Milli-Q water, and vacuum-dried at 70 °C for 5 h to yield the final catalyst. The same powder mixture was subjected to the same synthesis conditions but without the addition of $SmCl_3$ (the mole ratio of Ir, Sm, and CN_2H_2 was 5: 0: 80) for comparison. The heat treatment time of Ir$_2$Sm-S/G and Ir/G is 2 hours, and Ir$_2$Sm-L/G is 6 hours.

Electrochemical measurements

Electrochemical measurements were conducted on a CHI 660E Electrochemical Workstation (Shanghai Chenhua Instrument Corporation, China) in a conventional three-electrode cell. 2 mg synthesized catalysts were dispersed in a mixture of 490 µL ultrapure water, 490 µL isopropanol, and 20 µL Nafion solution, after sonication for 1 h. To ensure that the Ir content on the electrodes is similar, 3 mg of commercial Ir/C catalyst was used to prepare the ink. The graphite rod electrode is the counter electrode, a mercurous sulfate electrode is the reference electrode, and 0.5 M H_2SO_4 solution is the electrolyte. The working electrode was a glassy carbon electrode (GCE, diameter: 5 mm, area: 0.196 cm^2). Ten microliters of the catalyst were

dropped onto the GCE surface for further electrochemical tests. The potentials in this work were converted to a reversible hydrogen electrode (RHE) scale according to the Nernst equation ($E_{RHE} = E_{Hg/Hg2SO4} + 0.059$ pH $+ E^*_{Hg/Hg2SO4}$); the overpotential (η) was calculated according to the following formula: η (V) $= E_{RHE} - 1.23$ V. Oxygen evolution reaction (OER) performance was investigated by linear sweep voltammetry (LSV) at the scan rate of 5.0 mV s^{-1}. All the polarization curves were obtained with ohmic potential drop (iR) correction arising from the solution resistance. Ohmic losses were corrected by subtracting the ohmic voltage drop from the measured potential, using the electrolyte resistance determined by the electrochemical impedance spectroscopy (EIS) at a high-frequency where iR-corrected potentials were denoted as E- iR_s (i as the current and R_s as the electrolyte resistance). The Tafel slopes were derived from LSV curves at low overpotential fitted to the Tafel equation: $\eta = a + b \, logj$, where η is the overpotential, b is the Tafel slope, j is the current density, and a is the constant. The long-term stability of the catalyst was examined through chronopotentiometry at a constant current density of 10 mA cm^{-2} of the samples supported on the carbon cloth. Cyclic voltammetry (CV) curves were collected at different scan rates (5, 10, 15, 20, and 25 mV s^{-1}) in a non-Faradaic potential window, which was measured from 1.21 to 1.31 V (vs RHE). The double-layer capacitance (C_{dl}) was obtained by plotting current densities (Δj) at 1.26 V (vs RHE) against scan rates, and the linear slope is twice the value of the calculated C_{dl}, where Δj stands for the different current density between anode and cathode. The electrochemical active surface area (ECSA) was estimated from C_{dl} using the following equation: ECSA $= S \times C_{dl}/C_s$, where S and C_s (0.035 mF cm^{-2}) represent the geometric area and specific capacitance of the working electrodes, respectively. The mass activity was calculated from the current density and mass loading of electrocatalysts at 1.53 V (*vs* RHE). The mass activity and specific activity were normalized by the mass of Ir metal (determined by the ICP tests). Electrochemical impedance spectroscopy (EIS) measurements were measured at 1.50 V (vs RHE) in the frequency range from 100 kHz to 0.05 Hz with 5 mV amplitude in Ar saturated solution.

Physical characterization

The powder X-ray diffraction (XRD) measurements were carried out on Rigaku Smart Lab 3 kW, an X-ray diffraction diffractometer using monochromatized Cu Kα radiation (λ=1.5418 Å). X-ray photoelectron spectra (XPS) was conducted using a Thermo Scientific ESCALAB 250Xi instrument equipped with an Al X-ray excitation source. Transmission electron microscope (TEM) and high-angle annular dark-field scanning transmission electron

microscopy images(HAADF-STEM) and energy-dispersive spectroscopy (EDS) were obtained using a Field-emission transmission electron microscope (JEM-2800, JEM-ARM200F). The contents of the electrocatalyst were analyzed by Inductively Coupled Plasma Mass Spectrometry (Elan drc-e, USA).

DFT calculations

All DFT calculations were carried out by the Vienna ab initio Simulation Package (VASP).[1, 2] The Perdew-Burke-Ernzerhof (PBE)[3] exchange-correlation functional and projector augmented wave (PAW)[4] pseudopotential was adopted with spin-polarization. During the structure optimization, the convergence criterion of total energy was set to 10^{-5} eV, and the atoms were relaxed until the force acting on each atom was less than 0.01 eV/Å. Gaussian smearing of 0.05 eV to the orbital occupation is applied. A plane-wave cut-off energy of 500 eV was used in all computations. Brillouin-zone sampling was sampled with 3×3×1 Monkhorst-Pack grids. Each slab model was separated from its neighbors by 15 Å vacuum layer spacing. DFT-D3 method of Grimme with the zero-damping function was used in van der Waals (vdW) corrections.[5] The free energy profiles, which are efficient in estimating the performance of electrocatalytic reactions, were acquired by applying the computational electrode model (CHE).[6, 7] To accurately assess the OER activity of the alloys, we modeled the Ir_2Sm (111) and Ir (111) surfaces in combination with experimental characterization and enriched Ir atoms on the Ir_2Sm (111) surface. Taking into account the slight oxidation of the alloy surface, all DFT calculations were performed on the oxygen-covered surface (the atomic ratio of Ir to O was about 3:1).

The Gibbs free energies of the OER were calculated by correcting the DFT energy with zero-point energy and entropy via $\Delta G = \Delta E + \Delta ZPE - T\Delta S$, where E is the DFT total energy, ZPE is the zero-point energy, T is the environmental temperature (298.15 K), and S is the entropy. For zero-point energy correction and entropy calculations, the vibrational frequencies were calculated by employing density functional perturbation theory. Considering the effect of solvation, we corrected the adsorption energy by using VASPsol.[8]
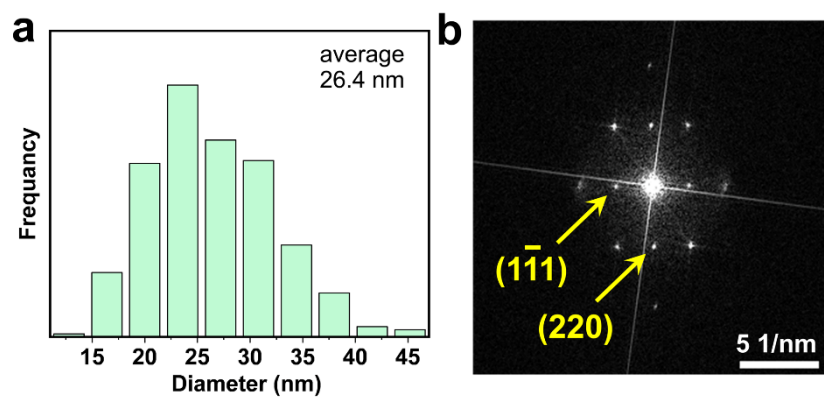
Figure S1. (a) Particle size distribution of Ir$_2$Sm-L/G, (b) FFT patterns of Figure 1f.
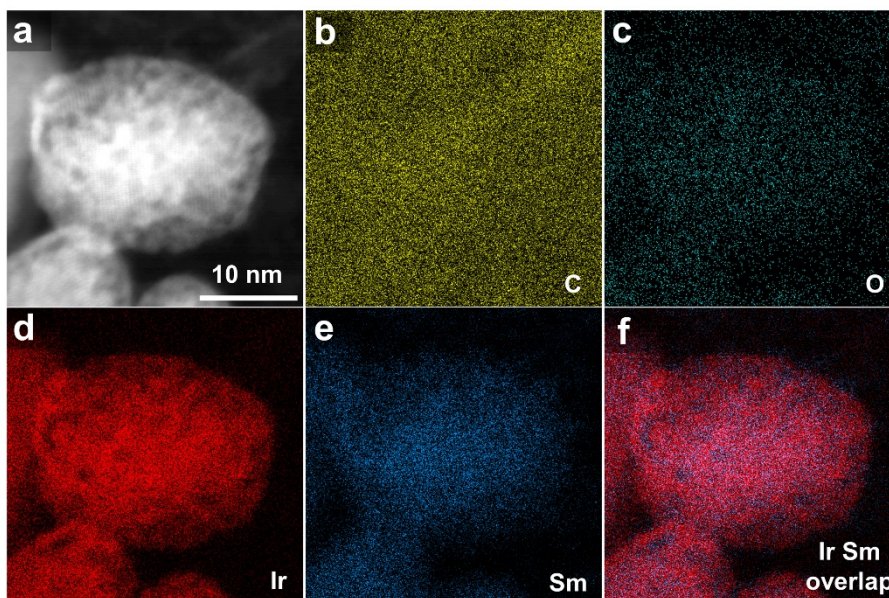
Figure S2. Element mapping of Ir$_2$Sm-L/G. (a) STEM image of Ir$_2$Sm-L/G, (b, c, d, e, f) the corresponding EDS elemental mappings.
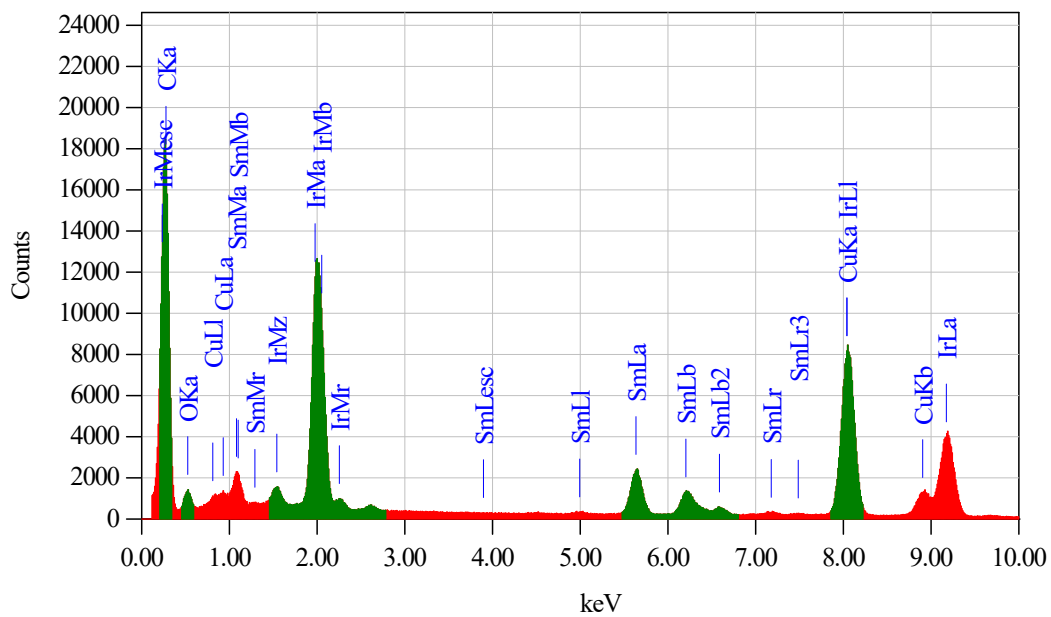
Figure S3. Element mapping spectrum of Ir$_2$Sm-L/G.
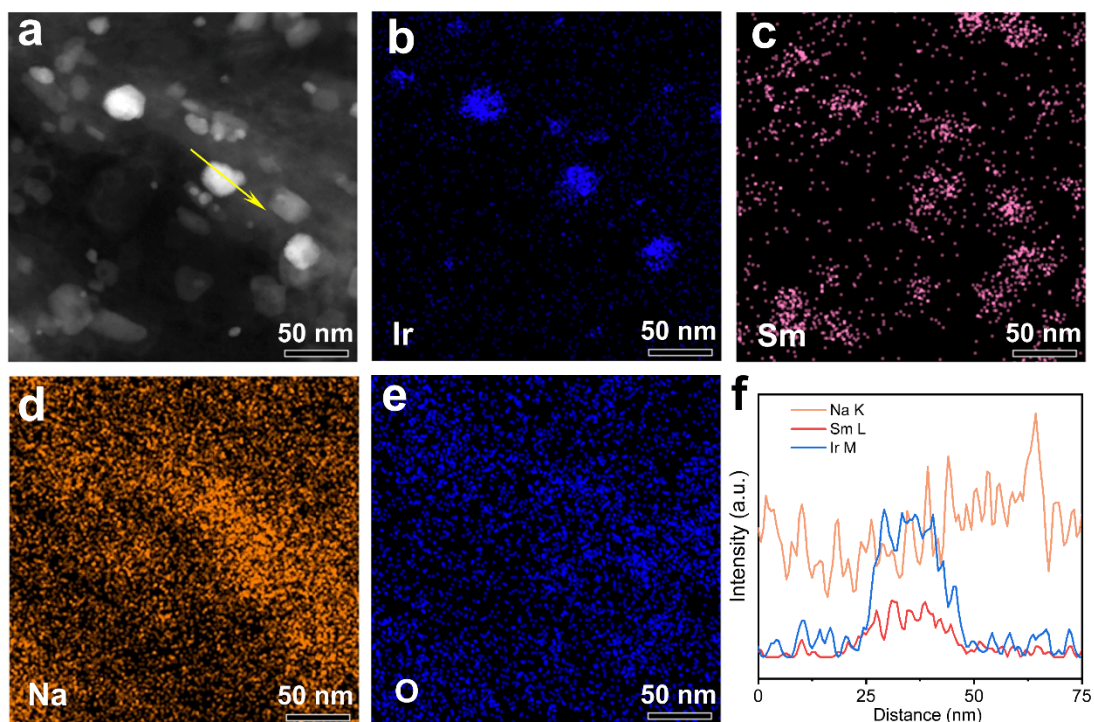
Figure S4. (a) STEM image of Ir$_2$Sm-L/G precursor, (b, c, d, e) the corresponding EDS elemental mappings, (f) STEM-EDS line scan taken along the atomic layers marked by the yellow arrows in (a).
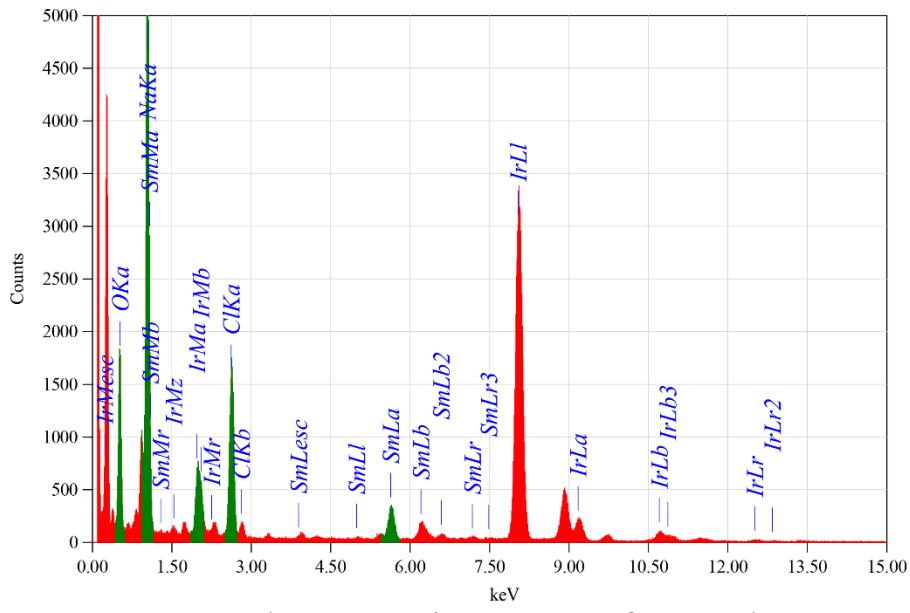
Figure S5. Element mapping spectrum of Ir$_2$Sm-L/G precursor.
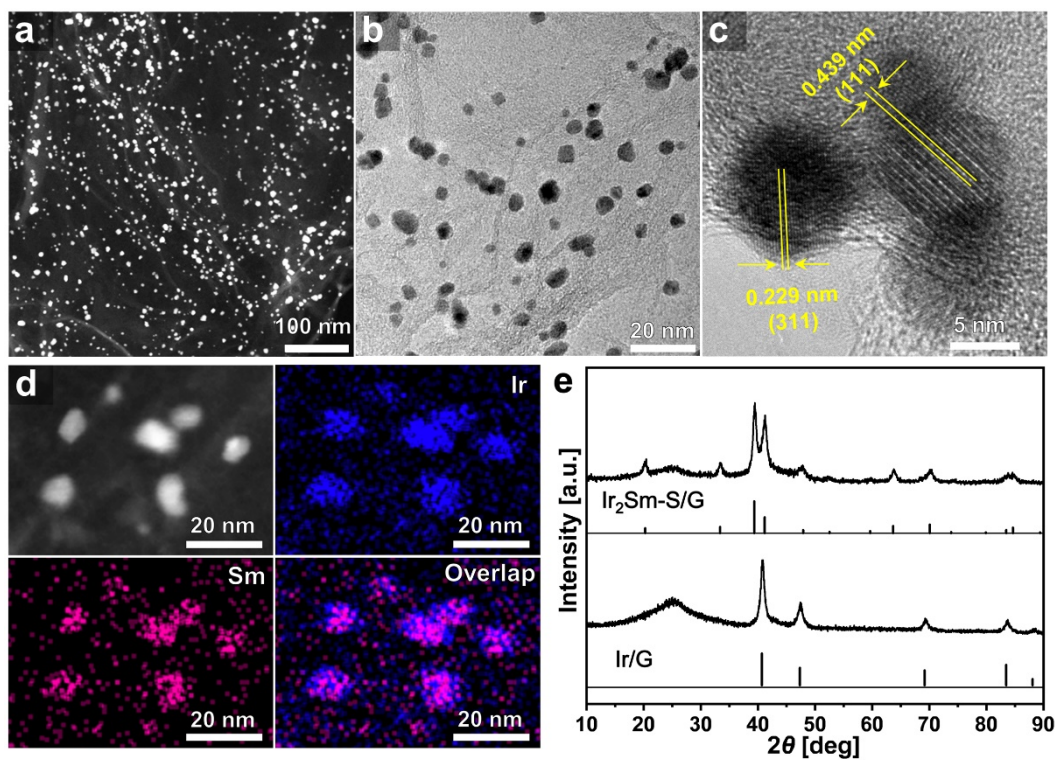
Figure S6. (a) STEM image of Ir_2Sm-S/G, (b) TEM image of Ir_2Sm-S/G, (c) high-resolution TEM image, (d) the corresponding EDX elemental mappings of Ir_2Sm-S/G, (e) XRD patterns of Ir_2Sm-S/G and Ir/G.
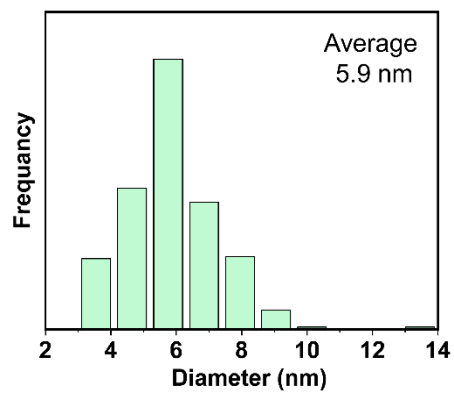
Figure S7. Particle size distribution of Ir$_2$Sm-S/G.
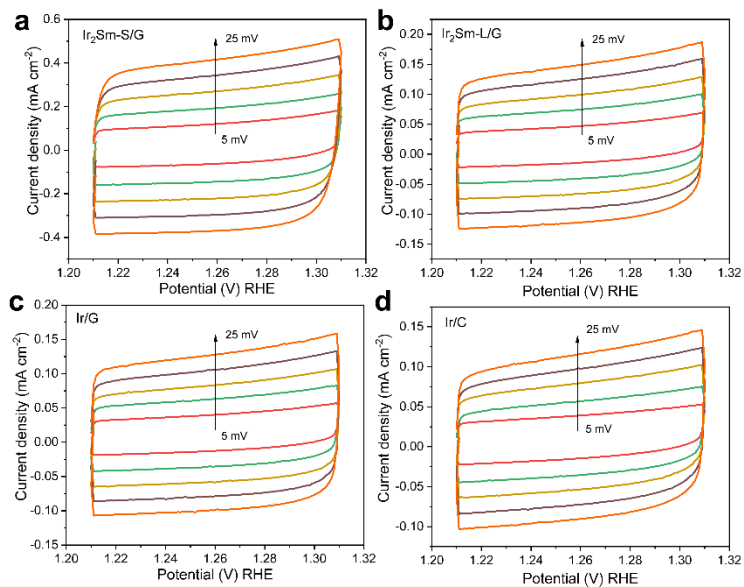
Figure S8. The CV curves of (a) Ir$_2$Sm-S/G, (b) Ir$_2$Sm-L/G, (c) Ir/G, (d) Ir/C at the range of 1.21 to 1.31 V with the scan rates from 5 to 25 mV s^{-1}.
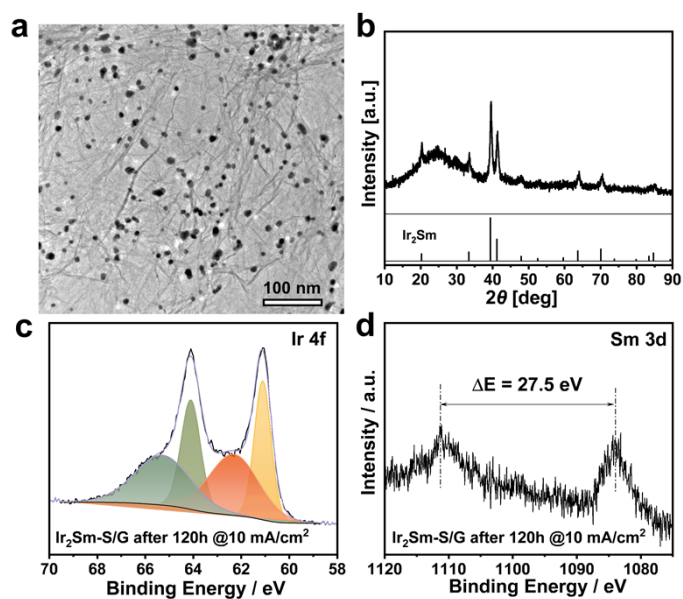
Figure S9. Characterization of the Ir$_2$Sm-S/G after long-term OER test. (a) TEM image, (b) XRD pattern, (c) high-resolution XPS spectra of Ir 4f orbitals, (d) high-resolution XPS spectra of Sm 3d orbitals.
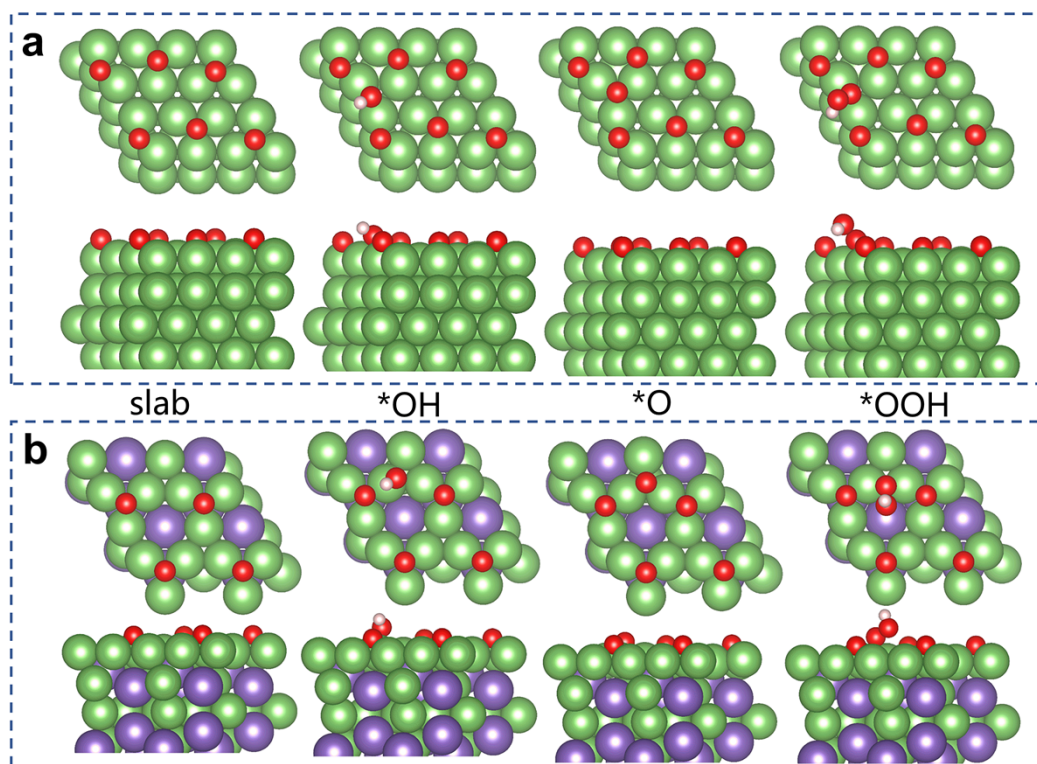
Figure S10. Optimized geometries of reaction adsorbates on the surfaces. (a) Ir(111), (b) Ir$_2$Sm(111), green, blue, red and white spheres are Ir, Sm, O and H atoms, respectively.

Table S1. Cell parameters of Ir_2Sm were determined from the XRD data.

	Ir_2Sm
Lattice type	F
Space group	Fd-3m
a, Å	7.5881
b, Å	7.5881
c, Å	7.5881
α	90.0°
β	90.0°
γ	90.0°

Table S2. The ICP data of Ir/G, Ir_2Sm-S/G, Ir_2Sm-L/G samples.

Catalysts	$Ir/_{wt}\%$	$Sm/_{wt}\%$	Stoichiometry
Ir/G	15.91	-	Ir
Ir_2Sm-L/G	14.14	5.44	$Ir_{2.01}Sm_{0.99}$
Ir_2Sm-S/G	14.39	5.32	$Ir_{2.04}Sm_{0.96}$

Table S3. Comparing the catalytic performance of Ir_2Sm-S/G samples with the Ir alloy OER catalysts.

Catalysts	Electrolyte	η (mV) @10 mA cm^{-2}	Mass activity (A mg$^{-1}_{Ir}$)	References
Ir_2Sm-S/G	0.5 M H_2SO_4	275	1.24	This work
$Rh_{22}Ir_{78}$	0.5 M H_2SO_4	292	1.17	9
DO-IrTe$_2$	0.5 M H_2SO_4	298	0.21@1.53 V	10
Pt-Ir frame	0.1 M $HClO_4$	308	0.64@1.53 V	11
IrNi NPNWs	0.1 M $HClO_4$	283	0.732@1.53 V	12
Ir/Fe$_4$N	0.5 M H_2SO_4	316	0.12@1.54 V	13
Ir$_3$Cu MAs	0.1 M $HClO_4$	298		14
P-IrCu$_{1.4}$ NCs	0.05 M H_2SO_4	311	0.21@1.55 V	15
IrNi/C	0.1 M $HClO_4$	290	1.5@1.53 V	16
IrNiCu	0.1 M $HClO_4$	303	0.46@1.53 V	17
Co-IrCu ONC	0.1 M $HClO_4$	293	0.64@1.53 V	18
IrCoNi	0.1 M $HClO_4$	303	~0.75@1.53 V	19
3D Ir	0.1 M $HClO_4$	270		20
IrNi TL	0.05 M H_2SO_4	350 (@ 5 mA cm^{-2})	0.50@1.51 V	21
IrO$_x$-Ir	0.5 M H_2SO_4	295	0.01@1.48 V	22
Cu$_{1.11}$Ir NCs	0.05 M H_2SO_4	286	0.07@1.51 V	23

Table S4. Solution resistance (R_s) and charge transfer resistance (R_{ct}) of Ir/C, Ir/G, Ir$_2$Sm-S/G, Ir$_2$Sm-L/G in 0.5 M H$_2$SO$_4$ electrolyte at 1.47 V vs. RHE.

Catalysts	R_s/Ω	R_{ct}/Ω
Ir/G	21.2	603.0
Ir/C	21.5	532.9
Ir$_2$Sm-S/G	19.2	157.5
Ir$_2$Sm-L/G	21.3	206.8

References

1. G. Kresse and J. Hafner, *Phys. Rev. B*, 1993, **47**, 558.

2. G. Kresse and J. Furthmüller, *Phys. Rev. B*, 1996, **54**, 11169.

3. J. P. Perdew, K. Burke and M. Ernzerhof, *Phys. Rev. Lett.*, 1996, **77**, 3865.

4. P. E. Blöchl, *Phys. Rev. B*, 1994, **50**, 17953.

5. S. Grimme, J. Antony and S. Ehrlich and H. Krieg, *J. Chem. Phys. B*, 2010, **132**, 154104.

6. J. K. Nørskov, J. Rossmeisl, A. Logadottir, L. Lindqvist, J. R. Kitchin, T. Bligaard and H. Jonsson, *J. Phys. Chem. B*, 2004, **108**, 17886-17892.

7. K. Mathew, R. Sundararaman, K. L. Weaver, T. A. Arias and R. G. Hennig, *J. Chem. Phys.*, 2014, **140**, 9519.

8. K. Mathew, V. S. C. Kolluru, S. Mula, S. N. Steinmann and R. G. Hennig, *J. Chem. Phys.*, 2019, **151**, 234101.

9. H. Guo, Z. Fang, H. Li, D. Fernandez, G. Henkelman, S. M. Humphrey and G. Yu, *ACS Nano*, 2019, **13**, 13225-13234.

10. Y. Pi, Y. Xu, L. Li, T. Sun, B. Huang, L. Bu, Y. Ma, Z. Hu, C. W. Pao and X. Huang, *Adv. Funct. Mater.*, 2020, **30***, 2004375.

11. S. Choi, J. Park, M. K. Kabiraz, Y. Hong, T. Kwon, T. Kim, A. Oh, H. Baik, M. Lee and S. Paek, *Adv. Funct. Mater.*, 2020, **30***, 2070253.

12. Y. Wang, L. Zhang, K. Yin, J. Zhang, H. Gao, N. Liu, Z. Peng and Z. J. Zhang, *ACS Appl. Mater. Inter.*, 2019, **11***, 39728-39736.

13. B. M. Tackett, W. Sheng, S. Kattel, S. Yao, B. Yan, K. A. Kuttiyiel, Q. Wu and J. Chen, *ACS Catal.*, 2018, **8**, 2615-2621.

14. Q. Shi, C. Zhu, H. Zhong, D. Su, N. Li, M. H. Engelhard, H. Xia, Q. Zhang, S. Feng, S. P. Beckman, D. Du and Y. Lin, *ACS Energy Lett.*, 2018, **3**, 2038-2044.

15. Y. Pi, J. Guo, Q. Shao and X. M. Huang, *Chem. Mater.*, 2018, **30**, 8571-8578.

16. Y. Pi, Q. Shao, P. Wang, J. Guo and X. Huang, *Adv. Funct. Mater.*, 2017, **27**, 1700886.

17. J. Park, Y. J. Sa, H. Baik, T. Kwon, S. H. Joo and K. Lee, *ACS Nano*, 2017, **11**, 5500-5509.

18. T. Kwon, H. Hwang, Y. J. Sa, J. Park, H. Baik, S. H. Joo and K. Lee, *Adv. Funct. Mater.*, 2017, **27**, 1604688.

19. J. Feng, F. Lv, W. Zhang, P. Li, K. Wang, C. Yang, B. Wang, Y. Yang, J. Zhou, F. Lin, G. C. Wang and S. J. Guo, *Adv. Mater.*, 2017, **29**, 1703798.

20. Y. Pi, N. Zhang, S. Guo, J. Guo and X. Huang, *Nano Lett.*, 2016, **16**, 4424-4430.

21. J. Lim, S. Yang, C. Kim, C. W. Roh, Y. Kwon, Y. T. Kim and H. Lee, *Chem. Commun.*, 2016, **52**, 5641-5644.

22. P. Lettenmeier, L. Wang, U. G. Schindler, P. Gazdzicki, N. A. Cañas, M. Handl, R. Hiesgen, S. S. Hosseiny, A. S. Gago and K. A. Friedrich, *Angew. Chem. Int. Ed.*, 2016, **55**, 742-746.
23. C. Wang, Y. Sui, G. Xiao, X. Yang, Y. Wei, G. Zou and B. Zou, *J. Mater. Chem. A*, 2015, **3**, 19669-19673.